Research Square

Preprints are preliminary reports that have not undergone peer review.
They should not be considered conclusive, used to inform clinical practice,
or referenced by the media as validated information.

NADH-DLEM-seq: A High-Fidelity Multimodal Platform Revealing Fiber-Type-Specific Metabolic and Transcriptional Remodeling in Sarcopenia

Bei Li

beili@ciomp.ac.cn

Changchun Institute of Optics, Fine Mechanics and Physics, Chinese Academy of Sciences

Fuyuan Chen

University of Chinese Academy of Sciences

Shi Chen

https://orcid.org/0009-0008-8905-4641

Meina Chen

Mengting Ming

Tao Xiong

Liang Peng

Yuntong Wang

Yue Qu

Xuan Yang

Article

Keywords: Laser Ejection Microdissection, Beam Shaping, Photomechanical ejection, Full-length single-cell sequencing, Skeletal muscle heterogeneity

Posted Date: March 26th, 2026

DOI: https://doi.org/10.21203/rs.3.rs-9027627/v1

License: This work is licensed under a Creative Commons Attribution 4.0 International License.
Read Full License

Additional Declarations: There is **NO** Competing Interest.

NADH-DLEM-seq: A High-Fidelity Multimodal Platform Revealing Fiber-Type-Specific Metabolic and Transcriptional Remodeling in Sarcopenia

Fuyuan Chen [1, 2], Shi Chen [3], Meina Chen [4], Mengting Ming [4], Tao Xiong [3], Liang Peng [1, 2], Yuntong Wang [1, 2], Yue Qu [5, *], Xuan Yang [3, *], Bei Li [1, 2, *]

[1] *State Key Laboratory of Advanced Manufacturing for Optical Systems, Changchun Institute of Optics, Fine Mechanics and Physics, Chinese Academy of Sciences, Changchun, 130033, China*

[2] *University of Chinese Academy of Sciences, Beijing, 100049, China*

[3] *College of Biosystems Engineering and Food Science, Zhejiang Key Laboratory of Agri-food Resources and High-value Utilization, Zhejiang University, Hangzhou, Zhejiang, 310058, China*

[4] *School of Ophthalmology & Optometry, Eye Hospital, Wenzhou Medical University, Wenzhou, 325027, China*

[5] *Haining High-tech Research Institute, Jiaxing, Zhejiang, 314408, China*

**Corresponding author. E-mail: yue.qu@hn-hti.org; yangxuan218@zju.edu.cn; beili@ciomp.ac.cn*

Unraveling the spatial heterogeneity of tissue microenvironments is essential for understanding complex pathologies like sarcopenia. However, existing spatial omics technologies often compromise between single-cell resolution, macromolecular integrity, and metabolic context. Here, we present "Donut" Laser Ejection Microdissection (DLEM), a high-throughput, non-contact spatial sampling platform. By integrating Spatial Light Modulator (SLM)-based vortex beam shaping with a metal-assisted ejection mechanism, DLEM achieves subcellular precision (5μm) and "cold-cutting" isolation, fundamentally eliminating thermal damage. This ensures superior RNA quality, maintaining >82.5% genome alignment rates even at the single-cell level. We developed a multimodal NADH-DLEM-seq workflow to link in situ metabolic phenotypes with transcriptomic profiles. Applying this to a murine model of chronic kidney disease (CKD)-induced sarcopenia, we dissected the distinct molecular trajectories of oxidative (Type I) and glycolytic (Type IIB) myofibers. We reveal a dichotomous response to stress: Type I fibers undergo profibrotic remodeling via collagen signaling activation, whereas Type IIB fibers exhibit pronounced catabolic atrophy and mitochondrial disassembly. These findings, obscured in bulk analyses,

underscore DLEM as a powerful tool for deciphering the metabolic-transcriptional coupling in aging and disease, offering precise targets for therapeutic intervention in sarcopenia.

Keywords: Laser Ejection Microdissection, Beam Shaping, Photomechanical ejection, Full-length single-cell sequencing, Skeletal muscle heterogeneity

1. Introduction

Deciphering cellular heterogeneity within complex tissue microenvironments is a central task for unraveling developmental programs, aging trajectories, and disease pathogenesis [1,2]. To establish intrinsic links between cellular function and spatial localization at single-cell resolution, precise in situ spatial sampling technologies have become a critical bridge between histopathology and deep molecular omics analyses [3]. Currently, the field of spatial biology is dominated by three major technological paradigms. The first comprises in situ capture–based approaches, exemplified by 10x Genomics Visium, which enable high-throughput spatial mapping over large tissue areas[4,5]. However, owing to the physical spacing constraints of capture arrays, these methods often fail to achieve true single-cell resolution[6]. The second paradigm consists of in situ imaging–based technologies, such as MERFISH, which achieve subcellular spatial resolution through multiplexed probe hybridization[7,8]. Despite their high spatial precision, the widespread adoption of these approaches is hindered by experimental complexity, limited target throughput, and demanding probe design requirements[9]. The third paradigm encompasses physical separation techniques, represented by laser microdissection (LMD)[10,11]. Owing to their ability to precisely isolate regions of interest (ROIs) based on morphological features, LMD-based methods are widely regarded as the “gold standard” for acquiring high-purity tissue microregions[10]. By preserving the intact physical structure of target cells or tissue domains, LMD enables compatibility with diverse downstream high-throughput analyses, including transcriptomics, proteomics, and metabolomics, making it an ideal tool for dissecting the multidimensional complexity of tissues[12].

Despite the irreplaceable spatial resolution offered by laser microdissection (LMD), its large-scale application remains constrained by fundamental technical bottlenecks, particularly the difficulty of simultaneously balancing sampling

throughput, spatial precision, and sample integrity[13]. Conventional LMD systems typically rely on adhesive capture or laser catapulting–based collection strategies, which involve multi-step and operationally complex workflows. These procedures are inherently low in efficiency and poorly suited for high-throughput omics studies. More critically, to compensate for limited collection efficiency, researchers are often forced to enlarge the dissection area, thereby compromising spatial precision. In addition, traditional laser cutting processes are accompanied by substantial photothermal effects; direct laser exposure and ablation can induce RNA thermal degradation, severely diminishing library complexity and gene detection sensitivity in downstream sequencing analyses[14,15].

Skeletal muscle epitomizes the challenge of spatial heterogeneity. As a metabolic powerhouse, it comprises an intricate mosaic of fiber types—slow-twitch oxidative (Type I) and fast-twitch glycolytic (Type IIB)—that exhibit distinct susceptibilities to aging and disease [16]. Sarcopenia, the age-related loss of muscle mass and function, is not a uniform process but a complex remodeling event where metabolic shifts and structural degradation occur asynchronously across fiber populations. Understanding this "metabolic-transcriptional uncoupling" requires technologies capable of isolating specific myofibers based on their functional state without perturbing their molecular content [17-19]. However, conventional laser microdissection (LMD) suffers from photothermal damage that degrades RNA, while capture-based spatial transcriptomics often lacks the resolution to distinguish adjacent myofibers in dense tissue [20,21].

To address these challenges, we developed a high-throughput and high-precision tissue microregion sampling platform, termed the “donut” laser-ejection microdissection system (DLEM). This system introduces a liquid-crystal spatial light modulator (SLM) for dynamic beam shaping, generating a vortex beam with a sharply defined annular profile and a central intensity null. By replacing the conventional Gaussian beam, DLEM achieves subcellular cutting precision down to 5μm. In parallel, a non-contact ejection mechanism based on a metal sacrificial layer is employed, in which laser-induced mechanical propulsion rather than direct photothermal ablation enables tissue separation, thereby effectively eliminating heat-induced damage to biological samples. To validate the technical performance and biological applicability of this platform, we integrated DLEM with NADH enzyme-activity–based metabolic imaging to establish a multimodal NADH-DLEM-seq analytical workflow. This approach enabled accurate reconstruction of the spatial metabolic signatures of Type I

and Type IIB muscle fibers in mouse skeletal muscle at single-cell resolution, and further revealed fiber-type–specific transcriptional remodeling under CKD-induced stress. Collectively, the DLEM platform combines high spatial resolution, high sampling throughput, and superior RNA preservation, providing a powerful technological foundation for precision medicine and for investigating cellular heterogeneity within complex tissue microenvironments.

2. Results

2.1 Construction of the DLEM System

To surmount the technical bottlenecks of traditional laser microdissection, we successfully constructed the "Donut" Laser Ejection Microdissection (DLEM) system. The core innovation of this system lies in the integration of Spatial Light Modulator (SLM)-based vortex beam shaping technology with a metal layer-assisted non-contact ejection mechanism. First, to address the issue of uneven energy distribution caused by zero-order diffraction in traditional beam shaping, the DLEM system employs a liquid crystal SLM as the core component to achieve dynamic control of the laser wavefront[22] (Fig.1A). In SLM-based holographic beam shaping, zero-order diffracted light is a common source of interference. By superimposing a blazed grating phase, we effectively eliminated zero-order light interference[23], thereby obtaining an ejection spot with concentrated energy and uniform boundaries (Fig. 1B). This vortex beam, possessing a "donut" morphology, confines laser energy exclusively to the cutting path at the cell periphery, while maintaining near-zero energy at the beam center. This ensures an absolutely pure cutting spot free of residual stray energy, guaranteeing no impact on tissue within the non-cutting path, thus achieving precise isolation of the target region.

To further elevate microdissection precision to the subcellular level while facilitating the rapid acquisition of micro-regions of varying sizes, we generated a continuously tunable vortex optical field with diameters ranging from 5 to 50μm by precisely modulating the topological charge of the phase map (Fig. 1C). This broad-range beam shaping endows the DLEM system with exceptional adaptability: the 5μm ultimate resolution is competent for fine subcellular-level dissection, ensuring precise targeting of rare cells or specific organelles; meanwhile, the 5–50μm adjustable spot mode is designed for the efficient capture of micro-regions of diverse dimensions. This tunable optical field design achieves micron-level resolution while optimizing beam shape to maintain edge smoothness and focus along the laser path, ensuring the precise

separation of target areas.

To validate the application potential of the DLEM system in spatial transcriptomics, we evaluated its spatial positioning accuracy and resolution capabilities. Through the acquisition of high-resolution microscopic images, the original spatial positional information of target cells is preserved after complete ejection and transfer. This allows for the correlation of data with its spatial location following downstream transcriptomic analysis, thereby elucidating the spatial distribution characteristics of the omics data (Fig. 1D).

To circumvent damage to biological samples caused by direct laser thermal ablation[13], we introduced a non-contact ejection strategy based on the principle of Laser-Induced Forward Transfer (LIFT). In this experimental setup, 10μm-thick tissue sections were adhered to glass slides coated with a 25 nm metallic aluminum layer. The 10μm thickness is comparable to the diameter of most mammalian cells, ensuring an approximate monolayer cross-section and avoiding cell overlap. Concurrently, the selected 20μm vortex beam diameter fully encompasses the range of typical target cells, ensuring complete single-cell capture. Upon identifying the target cell, the system applies a single laser pulse (532 nm). The metallic aluminum layer along the cutting path absorbs the laser energy and instantaneously vaporizes, generating a mechanical thrust that precisely ejects the target micro-region and transfers it to the collection device (Fig. 1E, S1). This non-contact ejection substitutes for traditional direct thermal ablation, ensuring a "cold environment" during the isolation process, thereby perfectly preserving the morphological structure and molecular integrity of the sample.

Furthermore, benefiting from the single-pulse ejection mechanism, the system achieves high operational efficiency. We recorded the real-time dissection process via high-speed microscopic imaging (Fig. S2, Video 1), revealing that the actual laser interaction time with a single target micro-region is on the order of nanoseconds. Combined with an automated stage, single sampling is controlled within 1 second. Compared to the low-throughput operation of traditional laser microdissection, which typically requires 10–15 seconds to isolate a single cell[12,24], this instantaneous separation mode not only enhances sampling throughput (>50 regions/minute, Video 2) but also significantly shortens the exposure time of biological samples at room temperature.

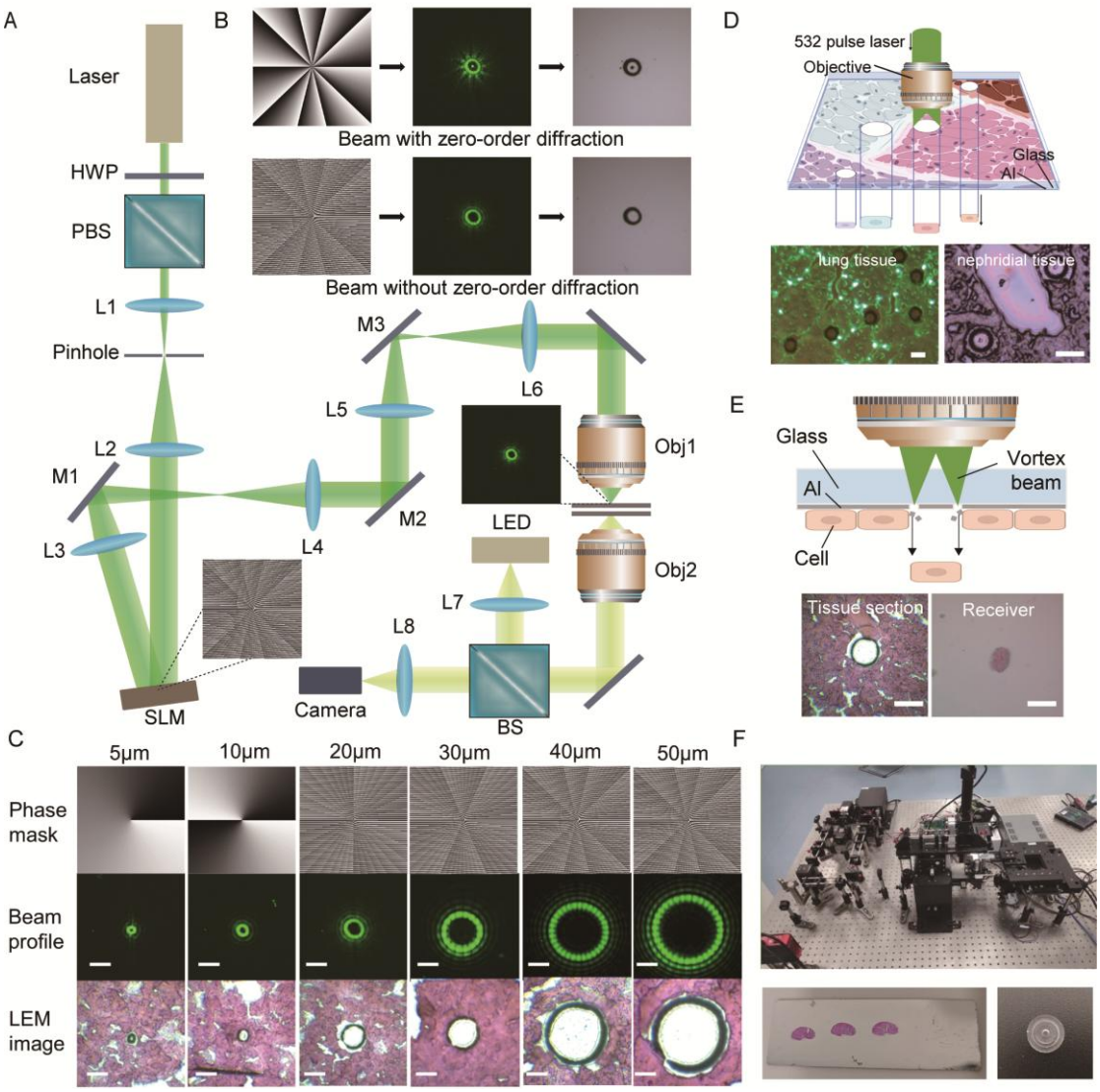


Figure 1. Construction and working principle of the "Donut" Laser Ejection Microdissection (DLEM) system. (A) Schematic diagram of the overall optical path. Key components include: Laser: MPL-N-532 (Changchun New Industries Optoelectronics Technology Co., Ltd.); SLM (Spatial Light Modulator): EXULUS-HD2 (Thorlabs); Obj1: 10×/NA 0.4 U Plan X Apo (Nikon); Obj2: 20×/NA 0.6 TU Plan ELWD (Nikon); L1: f = 15 mm, L2: f = 80 mm, L3–6: f = 150 mm, L7: ACL25416U-A, L8: f = 125 mm (Thorlabs); M1–5 (Mirrors): PF10-03-P01 (Thorlabs); HWP (Half-Wave Plate): WPHSM05-532 (Thorlabs); PBS (Polarizing Beam Splitter): PBS251 (Thorlabs); BS (Beam Splitter): BSW10R (Thorlabs); LED: MNWHD2 (Thorlabs); Camera: U3P630-H (Shenzhen DO3THINK Technology Co., Ltd.). (B) Comparison of zero-order diffraction suppression during vortex beam shaping. Top: Conventional holographic phase mask without the superposition of a blazed grating phase and its corresponding beam profile; distinct residual zero-order diffraction is visible at the center of the field of view. Bottom: After superimposing the blazed grating phase, the zero-order light is effectively eliminated, generating a "donut"-shaped vortex beam with a pure dark core. (C) Generation of vortex beams with continuously tunable diameters and their dissection

performance. Top row: Phase masks loaded onto the SLM. Middle row: Generated vortex beam profiles with diameters ranging from 5 to 50μm. Bottom row: High-precision dissection of corresponding tissue micro-regions. (D) Precise localization and isolation of target regions within complex tissues. The panel demonstrates the capability to trace back the original spatial positional information of the target unit after ejection. (E) Schematic (top) and microscopic images (bottom) of the metal sacrificial layer-assisted non-contact ejection mechanism. A 532 nm pulsed laser passes through the glass slide to interact with the 25 nm aluminum (Al) sacrificial layer, inducing instantaneous vaporization to generate propulsion thrust. This "ejects" the target cell into the receiver, thereby preventing direct thermal ablation of the biological sample. (F) Photograph of the physical DLEM system, alongside the ejection dissection chip and sample receiver. Scale bars: 20μm.

2.2 Performance Characterization of Laser Ejection Microdissection

Following the successful construction of the DLEM system, we systematically characterized its microdissection performance. To address the geometric diversity of target regions within complex biological samples, the DLEM system leverages the wavefront modulation capabilities of the SLM to achieve "on-demand tailoring" of beam shapes. In addition to conventional circular spots, we successfully generated sharp-edged rectangular and hexagonal vortex beams (Fig. 2A). This beam-shaping capability enables researchers to perform precise conformal sampling tailored to the native morphology of cells, thereby minimizing the inclusion of non-target regions. To quantitatively evaluate the dissection reliability of the system, we conducted arrayed sequential dissection experiments (Fig. 2B). Across two independent trials involving a total of 16 single-cell isolation operations, complete separation of the target cell was achieved in 15 instances, corresponding to a single-cell isolation success rate of 93.75% (15/16). Furthermore, we defined "edge integrity" as the complete separation of the target cell without visible tearing or deformation of the surrounding tissue, serving as a metric for dissection quality. Among all successfully isolated samples, the tissue edge integrity rate reached 100% (15/15) (Fig. 2C), indicating that DLEM possesses excellent stability and consistency under repetitive operational conditions.

Subsequently, we systematically evaluated the applicability of DLEM across various section thicknesses and sample types. The system demonstrated stable dissection performance across the 6μm to 16μm thickness range commonly used in cryosectioning (Fig. 2D). Attributable to the metal layer-mediated laser-induced ejection mechanism, DLEM effectively surmounts variations in tissue adhesion forces

across different thicknesses, achieving uniform ejection efficiency. Moreover, the application of this system is not limited to muscle tissue; we achieved precise sampling in various soft tissues—including mouse brain, kidney, liver, and lung—as well as highly adhesive bacterial biofilms (Fig. 2E), demonstrating superior sample compatibility.

Finally, we quantitatively characterized the system's ultimate spatial resolution and operational stability. In sequential dissection tests performed on mouse kidney tissue, DLEM exhibited subcellular-level spatial resolution, capable of precisely isolating adjacent micro-regions separated by gaps of less than 2μm (Fig. 2F). This micron-level positioning precision is critical for resolving closely packed cell subpopulations. In summary, the DLEM system demonstrates superior performance in terms of morphological flexibility, operational reliability, sample versatility, and micron-level precision, laying a solid technical foundation for subsequent high-throughput, low-damage single-cell sampling and molecular analysis.

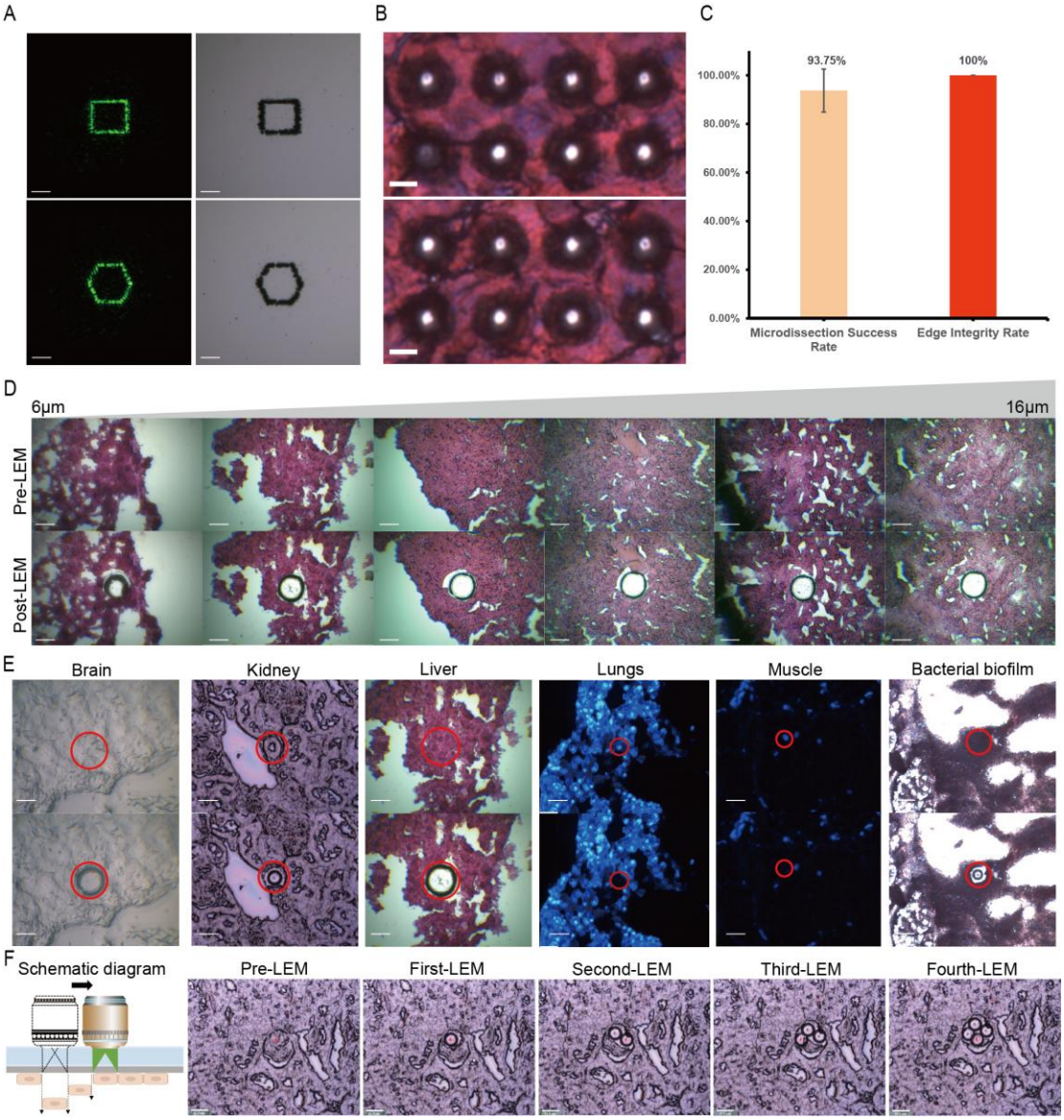


Figure 2. Performance characterization of the DLEM system. (A) Generation and application examples of multi-morphology dissection spots. Beyond conventional circular spots, the DLEM system generates rectangular and hexagonal vortex beams with sharp edges, achieving precise conformal dissection of irregular target regions. (B) Representative images of arrayed sequential dissection on H&E-stained cryosections, utilized to evaluate system stability and consistency under repetitive operational conditions. (C) Quantitative statistics of laser ejection microdissection performance. In arrayed single-cell dissection experiments, the single-cell isolation success rate was 93.8%, and the tissue edge integrity rate was 100%. (D) Dissection performance testing across varying tissue section thicknesses. The DLEM system demonstrates stable applicability for standard cryosection thicknesses ranging from 6 to 16μm. (E) Representative dissection examples across diverse biological sample types, including mouse brain, kidney, liver, lung, skeletal muscle tissues, and highly adhesive bacterial biofilms, demonstrating the system's broad sample compatibility. (F) Evaluation of microdissection spatial resolution. Sequential dissection experiments in mouse kidney tissue demonstrate that DLEM can stably isolate adjacent micro-

regions separated by gaps of less than 2μm. Scale bars: 20μm.

2.3 Establishment and Performance Evaluation of the Spatial Transcriptomic Workflow

While droplet-based single-cell platforms have established the gold standard for profiling naturally dissociated populations—such as circulating immune cells—they face inherent limitations when applied to structurally complex solid tissues. The novel DLEM-seq technology addresses this critical gap. Unlike conventional methods that rely on harsh enzymatic dissociation, which can induce stress responses or fail to isolate large, tightly packed cells, DLEM-seq enables the precise in situ acquisition of single cells. Although this approach offers no distinct advantage for free-floating cells, it is uniquely superior for investigating dense tissues like skeletal muscle. By bypassing the need for tissue disintegration, DLEM-seq preserves the molecular integrity of these difficult-to-isolate cells, making it an ideal tool for high-fidelity omics research in dense tissue environments (Fig. 3A).

Compared to traditional ultraviolet (UV) laser microdissection[25], DLEM employs a non-contact ejection mode based on a metal sacrificial layer. This effectively circumvents the direct impact of high temperatures and UV radiation on cells, thereby theoretically preserving the integrity of intracellular biological materials and ensuring the recovery of high-quality RNA from single cells or small cell clusters. To validate this hypothesis, we constructed and verified the "Imaging-Dissection-Sequencing" integrated DLEM transcriptomic workflow (Fig. 3B). This DLEM-seq workflow consists of the following steps: (1) 10μm-thick tissue sections are mounted onto aluminum-coated glass slides and fixed with paraformaldehyde; (2) high-resolution microscopic imaging is performed to precisely localize cell nuclei or predefined regions of interest; (3) target cells are non-contactly retrieved using our custom-built, automated DLEM platform, in which a vortex-beam-induced metal-layer ejection mechanism enables precise microregion recovery; (4) the collected minute samples are lysed and processed through the Smart-seq2 protocol for reverse transcription, amplification, and library construction; and (5) sequencing data are subjected to downstream transcriptomic bioinformatic analysis.

Performance Evaluation To systematically evaluate the performance boundaries of the platform under ultra-low input conditions, we performed DLEM-seq on 1, 5, and 10 cells, respectively. While traditional LMD technologies often require hundreds of cells to generate stable sequencing data[12], our results indicated that the DLEM system exhibits excellent stability and sensitivity at low input levels (Fig. 3C). Consistent laser dissection spot areas across biological replicates confirmed the reproducibility of beam

shaping (Fig. S3). cDNA yield showed a significant linear increase with cell number. The 10-cell group yielded the highest amount (521.9 ± 18.3 ng), significantly superior to the 5-cell (88.0 ± 9.2 ng) and single-cell (31.2 ± 2.6 ng) groups. Even at the single-cell level, cDNA yield was sufficient for high-quality library construction. The alignment rates to the Mouse Reference Genome Build 39 remained high across all samples (>83%), with the 10-cell group reaching 92.6 ± 0.3%. Compared to similar studies by Nichterwitz et al. [13], DLEM-seq demonstrated higher cDNA yields and superior sequence alignment performance at the single-cell level, further corroborating the significant advantages of this non-contact strategy in RNA integrity preservation.

Regarding gene detection sensitivity and quantitative accuracy, DLEM-seq performed exceptionally well. The number of detected genes exhibited a significant monotonic increasing trend as input increased from 1 to 5 and 10 cells (Fig. 3D). The average number of detected genes in single-cell samples reached 6,278 (2,158 high-expression genes with FPKM > 1), while the 5-cell and 10-cell samples increased to 7,057 (3,440 FPKM > 1) and 10,195 (6,298 FPKM > 1), respectively. These results indicate that even under trace input conditions, the method possesses extremely high transcript capture efficiency, with library complexity steadily improving as input increases. Correspondingly, the detection of high-confidence transcripts (Reads count > 10) significantly increased with cell number (Fig. 3E). Statistical analysis showed the 10-cell group was significantly higher than the 5-cell ($P=0.0007$) and single-cell ($P<0.0001$) groups. Furthermore, the sequencing saturation curve reached a plateau at low cell numbers, suggesting that the established sequencing depth sufficiently covered major transcripts. Spearman correlation analysis further revealed high consistency between the transcriptomic profiles of 10-cell and 5-cell samples (correlation coefficient approaching 1). Even single-cell samples maintained a strong positive correlation with multicellular samples (Fig. 3F), demonstrating that DLEM-seq retains good quantitative consistency and data reliability under ultra-low input conditions.

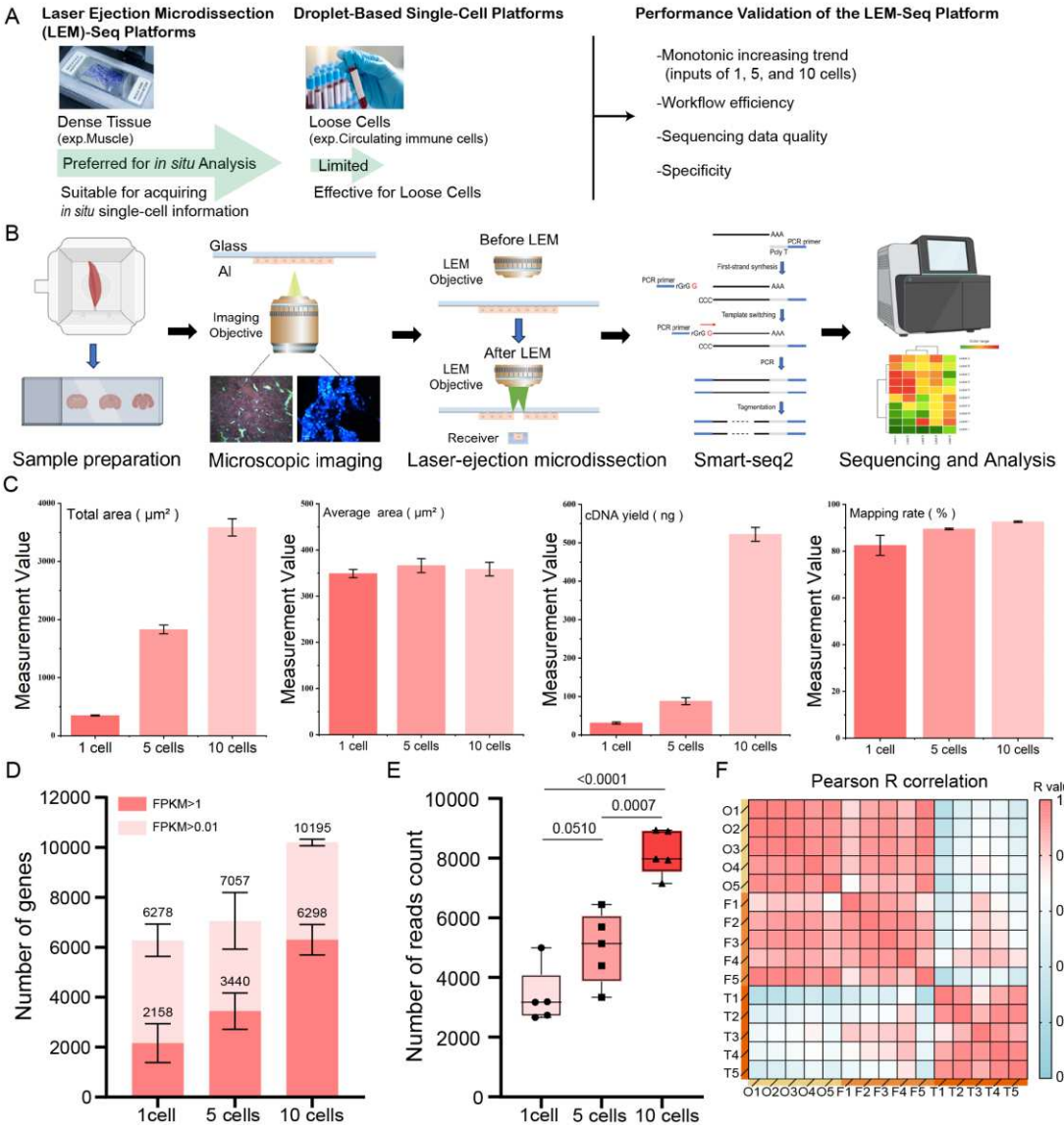


Figure 3. Performance evaluation of the DLEM-based spatial transcriptomics method. (A) Schematic comparison of the applicability of traditional droplet-based microfluidic single-cell sequencing platforms versus DLEM-seq technology. DLEM-seq acquires single cells in situ, thereby avoiding stress responses induced by enzymatic dissociation and the loss of large-volume cells. It is particularly suitable for the high-fidelity molecular analysis of structurally dense tissues such as skeletal muscle. (B) Schematic of the spatial transcriptomics workflow based on the DLEM platform, including cryosection preparation, microscopic imaging navigation, in situ laser ejection microdissection, sample recovery, and subsequent Smart-seq2 library construction and sequencing. (C) Quality assessment results of transcriptomic libraries derived from mouse skeletal muscle tissue cells constructed using the DLEM platform. (D) Average number of genes detected across groups with different cell numbers (presented as mean ± standard error). Stacked bar charts display the total number of genes detected in each group under different abundance thresholds (Light pink: FPKM > 0.01; Dark pink: FPKM > 1). Error

bars represent standard deviation (SD). (E) Average read counts detected across groups with different cell numbers. Data are presented as box plots with an abundance threshold of Reads count > 10. (F) Heatmap of gene expression correlation between samples. The color scale ranges from blue (low correlation) to red (high correlation, 1.0). O1–O5, F1–F5, and T1–T5 represent five biological replicates for sample groups containing 1, 5, and 10 cells, respectively. (Calculated using Spearman correlation coefficients; screening criteria included genes with expression levels ≥ 1 FPKM in at least one sample).

2.4 Histological Characterization and Construction of Metabolic Navigation Maps for Mouse Skeletal Muscle Pathology Models

To validate the capability of the DLEM system to identify specific cell subpopulations within pathological tissues and to establish a precise navigational basis for subsequent spatial transcriptomic sampling, we performed systematic histological characterization of mouse gastrocnemius muscle sections. First, Masson's trichrome staining was employed to evaluate histological structural changes in a purine-induced skeletal muscle senescent model (Fig. 4A). Histomorphological analysis revealed that, in contrast to the healthy group—which exhibited tightly packed myofibers and clear interstitium—the purine-induced senescent group displayed significant pathological alterations. These included markedly widened inter-myofiber spacing accompanied by substantial deposition of blue-stained collagen fibers. This characteristic fibrotic remodeling confirmed the successful establishment of a skeletal muscle injury model accompanied by metabolic decline, providing reliable biological specimens for investigating molecular mechanisms under pathological conditions.

Building on this, to achieve label-free targeted sorting of myofibers with distinct metabolic profiles, we utilized NADH staining technology (NADH-tetrazolium reductase stain) to construct an in situ metabolic navigation map of the tissue (Fig. 4B). This method differentiates myofibers based on variations in mitochondrial redox enzyme activity: Type I slow-twitch fibers, which are oxidatively active with high mitochondrial content, appear deep blue (NADH-high), whereas Type IIB fast-twitch fibers, which primarily rely on glycolysis, appear light blue (NADH-low). The results demonstrated that NADH staining clearly delineated the distribution characteristics of these two myofiber types in both healthy and injured tissues. This significant chromatic distinction served directly as an optical guidance signal for the DLEM system (Fig. S4). This enabled the precise localization and discrimination of functionally distinct

myofiber subpopulations without reliance on exogenous antibody labeling, thereby defining the target ROIs for laser microdissection.。

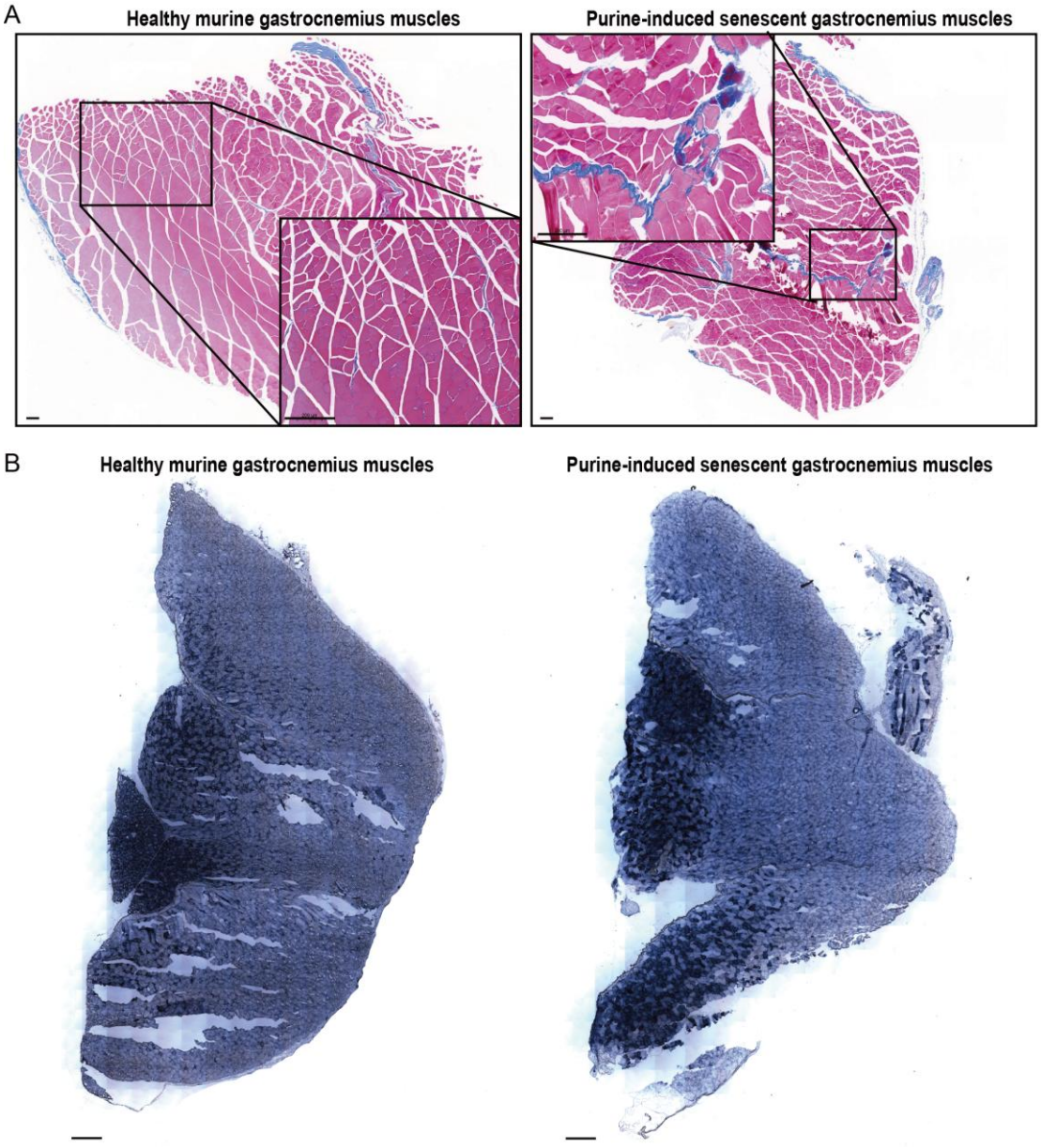


Figure 4. Pathological characterization and metabolic navigation of mouse skeletal muscle tissue. (A) Comparison of Masson's trichrome staining results in skeletal muscle sections from healthy controls versus the purine-induced senescent group. The senescent group exhibits distinct collagen fiber deposition (stained blue) and widened inter-myofiber spaces, reflecting characteristic fibrotic tissue remodeling. These features provide a histological basis for identifying the spatial distribution of different myofiber types. (B) In situ metabolic navigation maps constructed via NADH enzymatic activity staining. Leveraging differences in mitochondrial redox enzyme activity, myofibers with distinct metabolic profiles exhibit significant chromatic differentiation: Type I oxidative myofibers appear dark blue (NADH-

high), whereas Type IIB glycolytic myofibers appear light blue (NADH-low). This metabolic map requires no antibodies or exogenous labeling and serves directly as an optical navigation signal for the DLEM system, enabling the targeted microdissection of specific myofiber subpopulations. Scale bars: 200μm.

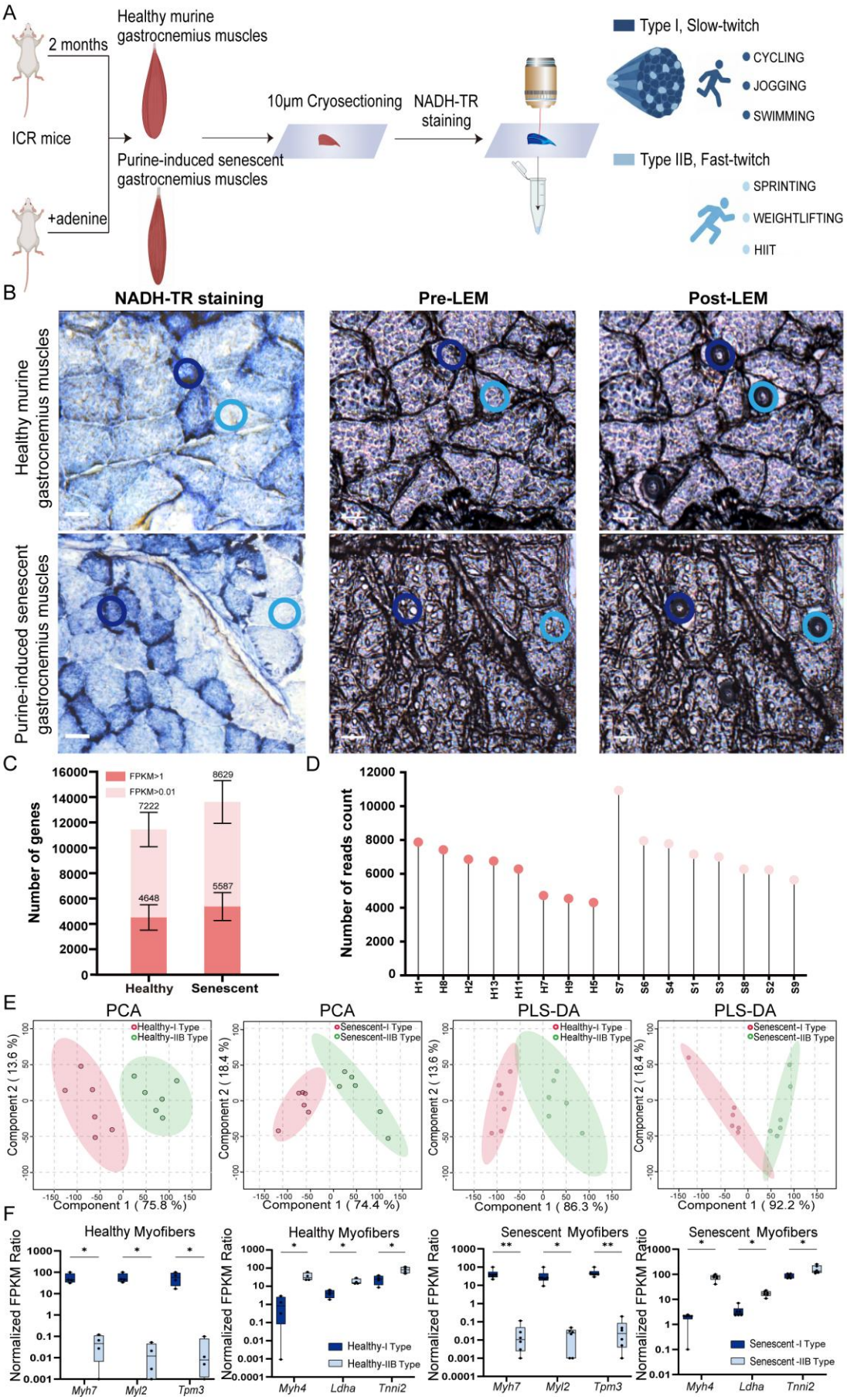
2.5 NADH-DLEM Reveals Metabolic-Transcriptional Coupling Characteristics of Myofiber Subpopulations

To deeply dissect the metabolic heterogeneity within the skeletal muscle microenvironment, we utilized the DLEM system to investigate molecular remodeling mechanisms in the mouse gastrocnemius muscle under homeostatic and stressed states (Fig. 5A). First, we established an purine-induced chronic kidney disease secondary muscle atrophy model to simulate the processes of muscle fibrosis and metabolic decline[26]. Guided by NADH staining, we precisely isolated oxidative (Type I, NADH-high) and glycolytic (Type IIB, NADH-low) myofibers from both healthy and purine-induced senescent mice, yielding four distinct sample groups for subsequent transcriptomic analysis. Leveraging the imaging guidance and non-contact ejection capabilities of the DLEM system, we achieved high-precision in situ isolation of these metabolically distinct myofiber subpopulations. Microscopic imaging results demonstrated that the DLEM system performed micron-level precision dissection along myofiber boundaries. The post-isolation tissue exhibited smooth-edged, structurally defined excision voids with no visible signs of thermal damage in the surrounding tissue (Fig. 5B), confirming the platform's suitability for high-fidelity sampling within complex tissue microenvironments.

Subsequently, we systematically evaluated the quality of the sequencing data. The results demonstrated that DLEM-seq maintained exceptional sensitivity and stability in both healthy and aging samples. Regarding gene detection (Fig. 5C), the mean number of genes detected in healthy samples reached 7,222 (4,648 highly expressed genes with FPKM > 1), whereas the number in aging samples was 8,629 (5,587 with FPKM > 1). These results indicate that despite potential microenvironmental deterioration in aging tissues, the DLEM system can still effectively capture a sufficient quantity of transcripts. Accordingly, we quantified the high-confidence transcripts (Reads count > 10) across the 16 samples (Fig. 5D). The results showed that the number of detected genes remained consistently above 5,000 in 81.25% of the samples. This demonstrates that despite the samples originating from different pathological states, the number of

detected genes exhibited high consistency. This stability in gene detection across samples and groups provides strong evidence for the robustness of the DLEM workflow, confirming that the capture efficiency of the technique is not subject to significant technical bias caused by differences in the pathological states of the samples.

Building on this, transcriptomic analysis clearly revealed a high degree of concordance between myofiber metabolic phenotypes and gene expression profiles. Principal Component Analysis (PCA) and Partial Least Squares Discriminant Analysis (PLS-DA) demonstrated that, in both healthy and purine-induced senescent states, the Type I and Type IIB fibers sorted by DLEM achieved complete separation at the molecular level, with no cross-contamination between samples (Fig. 5E). Differential gene expression analysis further validated the accuracy of the sorting: the dark blue regions (NADH-high) specifically expressed high levels of slow-twitch markers *Myh7*, *Myl2*, and *Tpm3*, while the light blue regions (NADH-low) were enriched for fast-twitch markers *Myh4*, *Ldha*, and *Tnni2* (Fig. 5F). These results indicate that NADH-guided DLEM-seq is capable of achieving precise coupled characterization of myofiber metabolic states and transcriptomic features within this workflow.



412 Figure 5. NADH-DLEM-seq Uncouples Divergent Fates of Myofibers in Sarcopenic Muscle (A)

Schematic illustration of the mouse skeletal muscle model construction and the NADH-DLEM multimodal analysis workflow. The experiment encompasses a healthy group and a purine-induced muscle aging/atrophy model. Myofibers were classified based on NADH enzymatic activity staining: Type I slow-twitch fibers, characterized by high mitochondrial content and active oxidative metabolism, exhibit high NADH activity (NADH-high); conversely, Type IIB fast-twitch fibers, which predominantly rely on glycolysis, exhibit low NADH activity (NADH-low). This classification reflects the metabolic heterogeneity of mitochondrial function within skeletal muscle under pathological states. (B) Representative microscopic images of the DLEM process. High- and low-metabolic activity myofiber subpopulations are precisely identified and dissected in situ based on the intensity of NADH staining (dark blue vs. light blue). Scale bar: 20μm. (C) Average number of genes detected in the healthy and purine-induced senescent groups (Mean ± SEM). (D) Counts of high-confidence transcripts detected in the 16 samples. H represents the healthy group; S represents the purine-induced senescent group. (E) Transcriptomic distribution characteristics of Type I and Type IIB myofiber subpopulations in healthy and purine-induced senescent skeletal muscle. Principal Component Analysis (PCA) and Partial Least Squares Discriminant Analysis (PLS-DA) demonstrate that myofibers of distinct metabolic types achieve clear molecular segregation across both physiological states, indicating that NADH-guided DLEM sampling possesses excellent sorting specificity. (F) Validation of representative marker gene expression across different myofiber subpopulations. In both healthy and purine-induced muscle, NADH-high regions exhibit significantly elevated expression of slow-twitch/oxidative metabolism-related genes (*Myh7, Myl2, Tpm3*), while NADH-low regions are specifically enriched for fast-twitch/glycolysis-related genes (*Myh4, Ldha, Tnni2*). Error bars represent Mean ± SEM; statistical significance was calculated using a two-sided t-test (*P < 0.05).

2.6 Transcriptomic Analysis Reveals Heterogeneity in Fibrosis Regulation Across Muscle Fiber Types

To investigate transcriptomic heterogeneity among different muscle fiber types following injury and to demonstrate the necessity of fiber-type–resolved analysis, we performed comprehensive transcriptomic profiling of 16 samples stratified by fiber type and injury status. Hierarchical clustering heatmaps (Fig. 6A, B) revealed markedly divergent gene expression profiles between Type I and Type IIB fibers after injury. Notably, when muscle tissue is analyzed as a homogeneous entity without fiber-type stratification, opposing or fiber-specific transcriptional changes between these two fiber types may counterbalance each other or remain obscured. In contrast, fiber-type–resolved analysis enabled by DLEM clearly delineated distinct response patterns unique to each fiber type, thereby establishing a foundation for understanding cellular heterogeneity within the fibrotic microenvironment.

To further characterize these differences, volcano plot analyses were employed to examine the global distribution of differentially expressed genes (DEGs) (Fig. 6C, D). The results revealed a pronounced disparity in the magnitude of transcriptional

responses between the two fiber types. In Type IIB fibers, a total of 1,055 significant DEGs were identified, including 905 upregulated and 150 downregulated genes, indicating a robust transcriptomic perturbation. In contrast, Type I fibers exhibited a comparatively moderate response, with 868 significant DEGs, of which 502 were upregulated and 366 were downregulated. These findings indicate that although both fiber types mount transcriptional responses to injury, they differ substantially in regulatory intensity and expression balance. To assess fiber-type–specific alterations in extracellular matrix remodeling and myofiber structural integrity, we further examined the expression patterns of canonical fibrosis markers *Fn1* and *Col1a1*, as well as the key sarcomeric structural protein *Ttn*. Unexpectedly, these genes exhibited divergent trends between the two fiber types. In Type IIB fibers, *Fn1* and *Col1a1* did not display the anticipated fibrotic upregulation; instead, both genes were significantly downregulated following injury. Concurrently, *Ttn*, which is essential for maintaining sarcomeric integrity, also showed marked downregulation. In contrast, Type I fibers exhibited only mild downregulation of *Fn1* and *Col1a1*, whereas *Ttn* was paradoxically upregulated. These results underscore the ability of fiber-type–resolved analysis to capture divergent gene expression responses that would otherwise be overlooked in bulk tissue analyses.

To elucidate the underlying biological pathways driving these fiber-type–specific differences in extracellular matrix remodeling after injury, Gene Ontology (GO) enrichment and KEGG pathway analyses were performed on the DEGs (Fig. 6E–H). Type I fibers were significantly enriched in transmembrane receptor protein serine/threonine kinase signaling pathways, as well as pathways associated with the positive regulation of collagen biosynthetic processes and collagen-activated signaling cascades. The activation of these collagen-related pathways suggests that Type I fibers retain a strong capacity for matrix remodeling following injury, thereby providing a permissive molecular environment for collagen deposition and muscle fibrosis. In contrast, the transcriptomic signature of Type IIB fibers predominantly reflected tissue breakdown, with significant enrichment in pathways related to muscle atrophy, regulation of ubiquitin-dependent proteolysis, and mitochondrial disassembly. This pronounced catabolic profile implies a constrained fibrotic progression in Type IIB fibers.

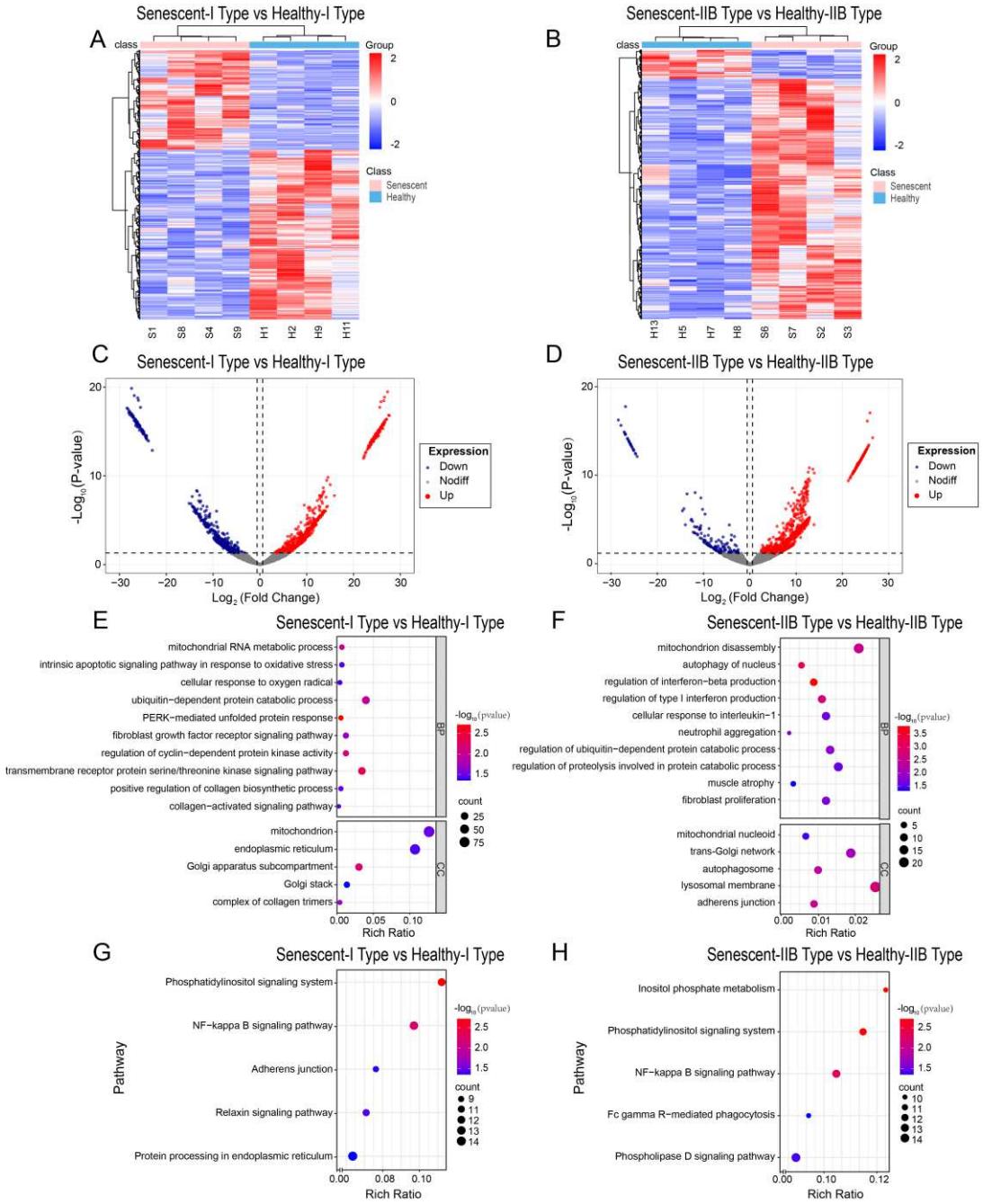


Figure 6. Transcriptomic analysis reveals heterogeneity in fibrosis regulation between Type I and Type IIB muscle fibers. (A, B) Fiber type–specific transcriptomic remodeling trajectories. Hierarchical clustering heatmaps of differentially expressed genes (DEGs) comparing the purine-induced senescent group with the healthy group in Type I (A) and Type IIB (B) muscle fibers. The color scale represents normalized gene expression levels, illustrating that under the same pathological condition, the two fiber types undergo markedly distinct molecular remodeling processes. (C, D) Volcano plots of differentially expressed genes. Gene expression changes following injury are shown for Type I (C) and Type IIB (D) fibers. Colored dots indicate statistically significant DEGs (FDR < 0.05), while darker dots denote core genes with large expression changes

(|log_2FC| > 1.5). Type IIB fibers exhibit a larger-scale transcriptomic perturbation than Type I fibers (1,055 DEGs vs. 868 DEGs), suggesting a higher sensitivity to injury. (E, F) Gene Ontology (GO) enrichment analysis of significantly differentially expressed transcripts. Bubble plots display representative biological processes and cellular components enriched in Type I and Type IIB muscle fibers. Dot color indicates statistical significance, and dot size represents the number of genes associated with each term. Statistical analyses were performed using the clusterProfiler R package with P values adjusted by the Benjamini–Hochberg method. (G, H) KEGG pathway enrichment analysis. Bubble plots visualize the six most significantly enriched signaling pathways in Type I and Type IIB muscle fibers. Dot size reflects the number of genes enriched in each pathway, while the color gradient indicates statistical significance. Enrichment analysis was conducted using the clusterProfiler package with Benjamini–Hochberg correction.

3. Discussion

Deciphering the spatial heterogeneity of complex tissues is pivotal for understanding development, disease progression, and aging mechanisms[1,2]. Although spatial transcriptomics technologies have witnessed rapid advancements in recent years, existing methods typically necessitate a trade-off between spatial resolution, detection throughput, and transcriptome coverage[27]. Array-based capture methods, while offering high throughput, are often constrained by resolutions of tens of micrometers, precluding analysis at single-cell precision[6]. Conversely, while traditional laser microdissection (LMD) possesses single-cell isolation capabilities, it is hampered by low throughput, laborious sample preparation workflows, and potential thermal damage induced by the laser[13]. The DLEM technology developed in this study successfully surmounts these bottlenecks through innovative optical path design and a laser ejection mechanism. We achieved a high spatial resolution of 5μm and an isolation throughput of 50 regions/minute. By integrating this with Smart-seq2 technology, we obtained high-quality, full-length transcriptomic data while preserving spatial positional information.

Compared to traditional LMD technologies, the core advantages of DLEM reside in its beam-shaping system and non-contact sample recovery strategy. Conventional ultraviolet (UV) laser cutting often induces carbonization at the cutting edge or RNA degradation due to continuous laser ablation[25]. In our system, we incorporated a liquid crystal Spatial Light Modulator (SLM) to generate sharp-edged vortex beams via holographic beam shaping technology, significantly enhancing the sharpness and precision of the dissection edge. Crucially, we introduced an ejection mechanism

assisted by a metal sacrificial layer (based on the LIFT principle). This strategy leverages the mechanical thrust generated by the metal layer's absorption of laser energy to "eject" the target cell, thereby avoiding direct laser interaction with the biological specimen and maximizing the preservation of RNA integrity. Our data corroborate that even with single-cell samples, DLEM yields high quantities of cDNA and a genome alignment rate exceeding 82.5%. This performance significantly surpasses traditional LMD methods, providing a reliable avenue for the deep sequencing of rare cell subpopulations.

Our study positions DLEM as a transformative tool for the precision medicine of muscle aging. Sarcopenia has long been difficult to treat due to the heterogeneity of muscle loss[16]. By establishing the NADH-DLEM-seq workflow, we demonstrate that metabolic state is a robust proxy for cell identity and functional trajectory in situ. The discovery that Type I fibers drive the fibrotic niche while Type IIB fibers undergo intrinsic wasting challenges the "one-size-fits-all" approach to muscle therapy. Future applications of DLEM could screen for drugs that specifically reverse mitochondrial disassembly in Type IIB fibers without exacerbating fibrosis in Type I regions. Furthermore, the "cold-cutting" capability of DLEM makes it uniquely suitable for analyzing senescent cells (which often have fragile, low-quality RNA) in aged human biopsies, bridging the gap between preclinical models and clinical pathology.

Despite the superior performance of DLEM in terms of precision and data quality, this study acknowledges certain limitations. First, as a microdissection-based technique, although the throughput of DLEM is significantly elevated compared to traditional LMD, it still lags behind whole-slide in situ sequencing technologies[4,7] regarding the comprehensive profiling of large-scale tissues. Consequently, DLEM is best positioned as a "targeted validation" tool—specifically, for conducting deep, full-length transcriptomic dissection after specific ROIs have been identified by other modalities. Second, the current system primarily relies on fluorescence or chromogenic labeling for guidance. Future integration of AI-assisted morphological recognition algorithms holds promise for achieving label-free, fully automated intelligent sampling. In summary, DLEM synergizes optical precision with biological fidelity, providing a robust platform to decode the cellular hierarchies of complex tissues. It opens new avenues for interrogating the "spatial metabolome-transcriptome" interface, essential for unraveling the mechanisms of sarcopenia and other age-related degenerative diseases.

4. Methods

4.1 Instrumentation of the DLEM System

A single-pulse laser operating at a wavelength of 532 nm with a pulse width of 1 ns (Full Width at Half Maximum, FWHM) was selected as the light source. The energy modulation module comprised a Half-Wave Plate (HWP) and a Polarizing Beam Splitter (PBS). To expand the laser beam, a beam expander consisting of Lens 1 and Lens 2 was employed, incorporating a pinhole for spatial filtering to minimize the influence of stray light. A phase-only reflective Liquid Crystal on Silicon Spatial Light Modulator (LCOS-SLM) was utilized, featuring a resolution of 1920 × 1080 pixels and an operating wavelength range of 400-850 nm[23]. It provided a phase retardation of at least 2pi at the 532 nm wavelength. Lenses 3–6 constituted two 4f optical relay systems. Mirrors (M1–M5) were used to steer the laser direction, and the modulated beam was directed into the ejection objective lens via these two sets of 4f systems. The implementation of the dual 4f system design was intended to accommodate spatial constraints while minimizing optical intensity loss[22]. The bottom imaging system, composed of a microscope objective and a CMOS camera, was employed for cellular image acquisition. The system supports both bright-field and fluorescence imaging modalities. For fluorescence observation, multi-channel detection was achieved via the automated switching of filter modules on a turret, supporting four channels: DAPI, GFP, Cy3, and Cy5.

4.2 Sample Preparation

Animal Husbandry and Grouping Male C57BL/6J mice (6–8 weeks old, weighing 20–22 g) were purchased from Vital River Laboratory Animal Technology Co., Ltd. (Beijing, China). All mice were housed in a Specific Pathogen-Free (SPF) barrier facility under strictly controlled environmental parameters: temperature 22 ± 2°C, humidity 50 ± 10%, with a 12-hour light/dark cycle. Mice were provided ad libitum access to sterile water and standard chow. All animal experimental protocols in this study strictly adhered to the National Guidelines for Animal Welfare and were reviewed and approved by the Animal Ethics Committee of Zhejiang University.

Following a one-week acclimatization period, mice were divided into two groups using simple random sampling (n=6 per group): Healthy Group: Fed a standard maintenance diet. purine-induced senescent Group: Fed a special diet supplemented

with 0.2% (w/w) adenine (Yuanye Bio-Technology, Shanghai) for 4–6 weeks to establish a model of Chronic Kidney Disease (CKD)-induced secondary skeletal muscle atrophy and fibrosis[26].

Skeletal Muscle Tissue Collection and Embedding At the experimental endpoint, mice were euthanized via cervical dislocation. To maximize the preservation of tissue RNA integrity, all dissection procedures were performed rapidly on ice. After peeling the hindlimb skin, bilateral gastrocnemius muscles were precisely isolated, and surface connective tissue and fat were carefully trimmed. The collected muscle tissues were trimmed to appropriate dimensions and oriented in molds containing OCT compound (Sakura Finetek, USA) such that the longitudinal axis of the myofibers was perpendicular to the base (to facilitate cross-sectional sectioning). Subsequently, the embedding molds were flash-frozen in liquid nitrogen until completely hardened. The resulting frozen samples were immediately transferred to a -80°C ultra-low temperature freezer for long-term storage, pending subsequent tissue sectioning and spatial transcriptomic analysis[21].

Chip Pretreatment and RNase Decontamination To strictly prevent RNA degradation during single-cell/spatial transcriptomic analysis, the DLEM sorting chip (or receiver device) underwent a standardized RNase decontamination procedure prior to use. The specific protocol was as follows: The chip was fully immersed in freshly prepared, pre-cooled PBS buffer supplemented with RNase Inhibitor (Beyotime Biotechnology, China; typically 7μL of 40 U/μL stock added to the wash solution) and washed with gentle agitation at 4°C for 30 seconds. After retrieving the chip, residual liquid on the surface was rapidly absorbed using cleanroom-grade lint-free wipes, and the chip was immediately subjected to the subsequent sample loading workflow[24].

4.3 Tissue Sectioning and Fixation

Cryosectioning Tissue sections (10μm thickness) were prepared using a cryostat and mounted onto metal-coated glass slides. To prevent the OCT embedding block from thawing during sectioning, the block was equilibrated within the cryostat chamber prior to use. Immediately following sectioning, slides were placed on dry ice to prevent freeze-thaw cycles and preserve RNA integrity. Fixation and Washing Tissue samples were subjected to 4% Paraformaldehyde (PFA) fixation. Specifically, tissue sections were incubated with 4% PFA on ice for 15 minutes. Subsequently, the sections were washed twice (1 minute per wash) using ice-cold PBS supplemented with RNase

Inhibitor (RI). Finally, the samples were allowed to air-dry on ice for 3 minutes before proceeding to downstream applications[28].

4.4 Preparation of RNase-free and Sterile Receivers

Circular receivers (4μL capacity) were placed into a 100 mL reagent bottle. The cleaning and sterilization protocol was performed as follows: Receivers were immersed in 1.5% sodium hypochlorite solution and soaked for 30 minutes. This step was repeated once with fresh solution. The solution was decanted, and the receivers were submerged in 75% ethanol. The bottle was placed on an orbital shaker at 200 rpm for 30 minutes. This washing step was repeated three times. The ethanol was removed, and the receivers were rinsed with sterile nuclease-free water. The bottle was agitated on an orbital shaker at 200 rpm. This rinsing step was repeated three times. After discarding the final supernatant, the bottle was shaken at 200 rpm for an additional 30 minutes to facilitate the removal of residual liquid. Using sterile forceps, the receivers were aseptically transferred into sterile Petri dishes (typically 5 units per dish). The dishes were placed in a biological safety cabinet with lids open and sterilized under UV irradiation overnight[29]. Finally, the dishes were sealed with Parafilm and stored until use. RNase-free PCR tubes were placed into sterile Petri dishes. The tube caps were aseptically removed by cutting along the tube wall. The tube bodies and caps were separated and sorted into distinct, clean Petri dishes. Prior to use, the components were subjected to decontamination in a UV crosslinker for 10 minutes.

4.5 Microscopic Imaging and Spatial Localization

Tissue sections were subjected to NADH staining to delineate regions exhibiting distinct metabolic states. Following the placement of the slide onto the stage, the specimen was visualized using the instrument's integrated microscopy system, and the specific scanning area was defined. Whole-slide imaging was performed using a 20× objective lens, and the resulting fields of view were seamlessly reconstructed via internal stitching algorithms. ROIs were subsequently designated based on specific research objectives.

4.6 Laser Ejection Microdissection and Collection

Cells were isolated from tissue sections mounted on metal-coated glass slides. An aluminum layer was deposited onto glass slides by sputter deposition, and localized laser irradiation was used to vaporize the Al layer, thereby ejecting the target cells from

the corresponding regions. By combining a pulsed laser with a metal absorption layer, cell separation was achieved without direct thermal damage to the biological sample. The laser beam was focused onto the specimen through the optical system to enable precise cutting, and the target region was ejected from the slide into a collection device. The laser pulse energy was set to 8μJ. During the sorting process, ultraviolet illumination was used for sterilization; the ambient temperature was maintained at 22–24 °C and the relative humidity at 40–65% to prevent sample desiccation. The collector was positioned directly beneath the sorting chip. Prior to sorting, bright-field images of the sample were recorded, and 4μL of oligo-tag solution was added to the collector. After sorting, images of the original position were acquired again, the collector was removed, capped tightly with a clean, treated PCR tube, and briefly centrifuged using a handheld centrifuge to transfer the liquid into the tube. Samples were then labeled and stored on ice for subsequent processing.

4.7 Smart-seq2 Library Construction

Smart-seq2 library preparation was performed according to established protocols with minor modifications[30,31]. PCR tubes were incubated in a thermal cycler at 50 °C for 15 min, followed by enzyme inactivation at 70 °C for 10 min. After incubation, 5.7 μL of reverse transcription reaction mix was added to the bottom of each tube, immediately placed on ice for 2 min, and then subjected to reverse transcription and template-switching amplification in a thermal cycler with 13 PCR cycles. For cDNA pre-amplification, 15μL of PCR amplification mix was added to 10μL of the reverse transcription product to yield a total volume of 25μL; the reaction was homogenized by pipetting up and down approximately 20 times, placed on ice for 2 min, and amplified with 28 PCR cycles. The amplified cDNA products were temporarily stored at −20 °C. For cDNA purification, magnetic beads were equilibrated to room temperature for 30 min, thoroughly mixed, and added to the DNA samples, followed by gentle pipetting to ensure complete mixing. After incubation at room temperature for 10 min to allow DNA binding, samples were placed on a magnetic rack and the supernatant was carefully removed once the solution became clear. The beads were washed twice with 200μL of freshly prepared 80% ethanol while remaining on the magnetic rack, air-dried at room temperature for 10 min with tube caps open, and subsequently resuspended in an appropriate volume of nuclease-free water. After incubation at room temperature for 2 min, samples were returned to the magnetic rack for 5 min, and approximately half of the cleared supernatant containing purified cDNA was transferred to a new nuclease-

free tube. Purified cDNA was stored at −80 °C until further use.

4.8 Sequencing and Bioinformatics Analysis

Illumina sequencing was performed on an Illumina MiSeq platform, and the resulting sequencing data were analyzed using bioinformatics pipelines.

A rigorous quality control procedure was applied to the raw sequencing data to ensure the reliability of downstream analyses. Adapter-containing reads were removed using Cutadapt, reads with an unknown base (N) content greater than 5% were discarded, and low-quality reads in which bases with a Phred quality score below 15 accounted for more than 40% of the total read length were filtered out. The resulting high-quality clean data were retained for subsequent analyses, and sequencing quality was assessed by calculating Q20, Q30, and GC content metrics. Clean reads were then aligned to the mouse reference genome using HISAT2, which employs a graph-based alignment algorithm to enable efficient and accurate mapping of RNA-seq reads, particularly across exon–exon splice junctions[32].

Transcript assembly and gene expression quantification were performed using StringTie based on the alignment results. Differential expression analysis between purine-induced senescent and healthy groups was conducted separately for Type I and Type IIB muscle fibers using the DESeq2 R package. DESeq2 models count data using a negative binomial distribution and is well suited for differential analysis of datasets with biological replicates[33]. P values were adjusted for multiple hypothesis testing using the Benjamini–Hochberg procedure. Genes with an adjusted P value < 0.05 and an absolute $\log_2$ fold change $|\log_2\text{FoldChange}| > 1.5$ were defined as significantly differentially expressed genes.

To investigate the biological functions of the differentially expressed genes, Gene Ontology (GO) enrichment analysis was performed using the clusterProfiler R package[34]. This analysis encompassed the three GO domains: biological process, cellular component, and molecular function. P values were calculated using a hypergeometric test and adjusted for multiple hypothesis testing with the Benjamini–Hochberg method. GO terms with an adjusted P value < 0.05 were considered significantly enriched.

To further elucidate the signaling pathways and metabolic processes associated with the differentially expressed genes, KEGG pathway enrichment analysis was

performed using the clusterProfiler R package. Differentially expressed genes were mapped to the KEGG database, and the statistical significance of gene enrichment in each pathway was evaluated using a hypergeometric test[35]. The Benjamini–Hochberg method was applied to control the false discovery rate, and pathways with a Q value < 0.05 were defined as significantly enriched signaling pathways.

4.9 Automation platform and throughput evaluation

The system integrates a motorized stage, laser control, camera acquisition, and receiver coordination to realize a fully automated "imaging–cutting–ejection–collection–recording" closed-loop workflow. The cutting and collection of a single ROI can be completed in less than 5 seconds, and a 96-sample experiment can be finished within 8 minutes. Users operate the control software to select cells or ROIs for automated processing.

Credit authorship contribution statement

Fuyuan Chen: Investigation, Formal analysis, Data Curation, Writing - Original Draft, Writing - Review & Editing. Shi Chen: Conceptualization, Writing - review & editing. Meina Chen: Conceptualization, Data curation. Mengting Ming: Conceptualization, Resources. Tao Xiong: Formal analysis, Data curation. Liang Peng: Methodology, Writing - Review & Editing. Yuntong Wang: Formal analysis, Writing – review & editing. Yue Qu: Writing - Review & Editing, Methodology. Xuan Yang: Conceptualization, Formal analysis, Data Curation, Writing - Review & Editing, Methodology. Bei Li: Conceptualization, Methodology, Writing - review & editing.

Declaration of Competing interest

The authors declare that they have no known competing financial interests or personal relationships that could have appeared to influence the work reported in this paper.

Data availability

Data will be made available on request.

Acknowledgments

The authors are grateful for the support from the National Natural Science Foundation of China (Grant No. 62304222； No.32302053).

References

1 Wu, Y. *et al.* Spatiotemporal immune landscape of colorectal cancer liver metastasis at single-cell level. *Cancer discovery* **12**, 134-153 (2022).

2 Hunter, M. V., Moncada, R., Weiss, J. M., Yanai, I. & White, R. M. Spatially resolved transcriptomics reveals the architecture of the tumor-microenvironment interface. *Nature communications* **12**, 6278 (2021).

3 Marx, V. Method of the Year: spatially resolved transcriptomics. *Nature methods* **18**, 9-14 (2021).

4 Ståhl, P. L. *et al.* Visualization and analysis of gene expression in tissue sections by spatial transcriptomics. *Science* **353**, 78-82 (2016).

5 Stickels, R. R. *et al.* Highly sensitive spatial transcriptomics at near-cellular resolution with Slide-seqV2. *Nature biotechnology* **39**, 313-319 (2021).

6 Lee, J., Yoo, M. & Choi, J. Recent advances in spatially resolved transcriptomics: challenges and opportunities. *BMB reports* **55**, 113 (2022).

7 Wang, G., Moffitt, J. R. & Zhuang, X. Multiplexed imaging of high-density libraries of RNAs with MERFISH and expansion microscopy. *Scientific reports* **8**, 4847 (2018).

8 Codeluppi, S. *et al.* Spatial organization of the somatosensory cortex revealed by osmFISH. *Nature methods* **15**, 932-935 (2018).

9 Huang, Q. *et al.* The frontier of live tissue imaging across space and time. *Cell Stem Cell* **28**, 603-622 (2021).

10 Nichterwitz, S., Benitez, J. A., Hoogstraaten, R., Deng, Q. & Hedlund, E. in *RNA Detection: Methods and Protocols* (ed Imre Gaspar) 95-110 (Springer New York, 2018).

11 Kim, S. *et al.* PHLI-seq: constructing and visualizing cancer genomic maps in 3D by phenotype-based high-throughput laser-aided isolation and sequencing. *Genome Biology* **19**, 158 (2018). https://doi.org/10.1186/s13059-018-1543-9

12 Datta, S. *et al.* Laser capture microdissection: Big data from small samples. *Histology and histopathology* **30**, 1255 (2015).

13 Nichterwitz, S. *et al.* Laser capture microscopy coupled with Smart-seq2 for precise spatial transcriptomic profiling. *Nature communications* **7**, 12139 (2016).

14 Vanderburg, C. R. & Clarke, M. S. Laser capture microdissection of metachromatically stained skeletal muscle allows quantification of fiber type specific gene expression. *Molecular and cellular biochemistry* **375**, 159-170 (2013).

15 Garcés-Schröder, M. *et al.* Characterization of skeletal muscle passive mechanical properties by novel micro-force sensor and tissue micro-dissection by femtosecond laser ablation. *Microelectronic Engineering* **192**, 70-76 (2018).

16 Schiaffino, S. & Reggiani, C. Fiber types in mammalian skeletal muscles. *Physiological reviews* **91**, 1447-1531 (2011).

17 Joanisse, S., Nederveen, J. P., Snijders, T., McKay, B. R. & Parise, G. Skeletal muscle regeneration, repair and remodelling in aging: the importance of muscle stem cells and vascularization. *Gerontology* **63**, 91-100 (2016).

18 Mancinelli, R. *et al.* Biological aspects of selected myokines in skeletal muscle: focus on aging. *International journal of molecular sciences* **22**, 8520 (2021).
19 Larsson, L. *et al.* Sarcopenia: aging-related loss of muscle mass and function. *Physiological reviews* **99**, 427-511 (2019).
20 Lindholm, M. E. *et al.* The human skeletal muscle transcriptome: sex differences, alternative splicing, and tissue homogeneity assessed with RNA sequencing. *The FASEB Journal* **28**, 4571-4581 (2014).
21 Soule, T. G. *et al.* A protocol for single nucleus RNA-seq from frozen skeletal muscle. *Life Science Alliance* **6** (2023).
22 Jesacher, A., Bernet, S. & Ritsch-Marte, M. Broadband suppression of the zero diffraction order of an SLM using its extended phase modulation range. *Optics express* **22**, 17590-17599 (2014).
23 Yang, Y., Forbes, A. & Cao, L. A review of liquid crystal spatial light modulators: devices and applications. *Opto-Electronic Science* **2**, 230026-230021-230026-230029 (2023).
24 Espina, V. *et al.* Laser-capture microdissection. *Nature protocols* **1**, 586-603 (2006).
25 Gallagher, R. I., Blakely, S. R., Liotta, L. A. & Espina, V. in *Molecular Profiling: Methods and Protocols* 157-178 (Springer, 2011).
26 Tamaki, M. *et al.* Chronic kidney disease reduces muscle mitochondria and exercise endurance and its exacerbation by dietary protein through inactivation of pyruvate dehydrogenase. *Kidney international* **85**, 1330-1339 (2014).
27 Wang, X., He, Y., Zhang, Q., Ren, X. & Zhang, Z. Direct comparative analyses of 10X genomics chromium and smart-seq2. *Genomics, proteomics & bioinformatics* **19**, 253-266 (2021).
28 Bussolati, G., Annaratone, L., Medico, E., D'Armento, G. & Sapino, A. Formalin fixation at low temperature better preserves nucleic acid integrity. *PLoS One* **6**, e21043 (2011).
29 Green, M. R. & Sambrook, J. How to win the battle with RNase. *Cold Spring Harbor Protocols* **2019**, pdb. top101857 (2019).
30 Picelli, S. *et al.* Smart-seq2 for sensitive full-length transcriptome profiling in single cells. *Nature methods* **10**, 1096-1098 (2013).
31 Picelli, S. *et al.* Full-length RNA-seq from single cells using Smart-seq2. *Nature protocols* **9**, 171-181 (2014).
32 Kim, D., Paggi, J. M., Park, C., Bennett, C. & Salzberg, S. L. Graph-based genome alignment and genotyping with HISAT2 and HISAT-genotype. *Nature biotechnology* **37**, 907-915 (2019).
33 Love, M. I., Huber, W. & Anders, S. Moderated estimation of fold change and dispersion for RNA-seq data with DESeq2. *Genome biology* **15**, 550 (2014).
34 Wu, T. *et al.* clusterProfiler 4.0: A universal enrichment tool for interpreting omics data. *The innovation* **2** (2021).
35 Kanehisa, M., Furumichi, M., Tanabe, M., Sato, Y. & KEGG, K. M. New perspectives on genomes, pathways, diseases and drugs., 2017, 45, pp. *D353-D361. DOI: https://doi. org/10.1093/nar/gkw1092*

Supplementary Files

This is a list of supplementary files associated with this preprint. Click to download.

- SupplementaryMaterial.docx